ISIJ International, Vol. 60 (2020), No. 8, pp. 1610–1616

MnS Precipitation Behavior in MnO–SiO_2 Inclusion in Fe–Mn–Si–O–S Alloy System at Solid-Liquid Coexistence Temperature

Jonah GAMUTAN,* Takahiro MIKI and Tetsuya NAGASAKA

Department of Metallurgy, Graduate School of Engineering, Tohoku University, Sendai, 980-8579 Japan.

(*Received on December 5, 2019; accepted on January 15, 2020*)

With the emerging significance of creating an acicular ferrite microstructure to provide an optimum set of properties in steel, MnS precipitation behavior on a MnO–SiO_2 inclusion at the solid-liquid coexistence temperature was experimentally investigated and thermodynamically elucidated in this study. Using a direct method of forming inclusions, alloy samples with varying sulfur concentrations [Fe-1.1Mn-0.10Si-0.05O-S (initial mass%); 0.005 to 0.031 initial mass% S] were prepared by holding at the solid-liquid coexistence temperature for 1 hour.

In samples with less than 0.011 mass% sulfur, the formation of a MnO–SiO_2 inclusion with a SiO_2-rich precipitate was observed. Formation of SiO_2 was described as a consequence of silicon enrichment in the liquid phase, which, under appropriate thermodynamic conditions, homogeneously precipitated and later on coalesced with the primary MnO–SiO_2 phase. On the other hand, in samples with more than 0.022 mass% sulfur, heterogeneous precipitation of MnS along the boundary of the primary MnO–SiO_2 inclusion and the alloy matrix was observed. Also, the SiO_2-rich phase was found to disappear with increasing sulfur addition. Since the likelihood of heterogeneous nucleation is higher than homogeneous nucleation, it was assumed that MnS precipitation on the surface of the primary MnO–SiO_2 prevented the secondary SiO_2-rich inclusion from coalescing with the existing MnO–SiO_2 inclusion. This was also further validated for solute enrichment in the liquid phase, wherein MnS precipitation temperature was found to shift to higher temperatures in alloys with higher sulfur content.

KEY WORDS: MnS precipitation; acicular ferrite; solid-liquid coexistence temperature; microsegregation.

1. Introduction

Formation of non-metallic inclusions in steels has been largely considered as detrimental to steel properties such as ductility, strength and corrosion resistance.[1–3] In 1990, the paradigm towards non-metallic inclusions shifted when Takamura and Mizoguchi introduced the concept of "Oxide Metallurgy", which emphasizes on the use of suitable oxide inclusions as heterogeneous nucleation sites of acicular ferrite during solidification.[4] At present, it is already generally accepted that steels with a high volume fraction of acicular ferrite provide an excellent combination of steel properties. Acicular ferrite nucleates heterogeneously on non-metallic inclusions during the transformation from austenite to ferrite resulting in a chaotic assembly of crystallographically disoriented laths. This leads to the typical fine-grained and interlocking structure of acicular ferrite, which makes it more difficult for the propagation of cleavage cracks in the alloy. Hence, an increase in strength and toughness can be expected with an increase in the amount of acicular ferrite in steel.[5–11]

Several mechanisms to promote nucleation of acicular ferrite have been suggested. These include a reduction of the interfacial energy for heterogeneous nucleation,[12–15] minimization of lattice mismatch to enhance ferrite nucleation,[16] introduction of thermal strains associated with the difference in thermal expansion coefficients,[17,18] and nucleation arising from localized depletion of solute elements near the inclusion.[19–23] Amongst all of these, it is universally recognized that complex inclusions, especially oxide inclusions precipitated with MnS, are the most efficient in promoting the nucleation of an acicular ferrite microstructure in steels.[24] This can be explained by the simultaneous action of a low mismatch strain between the oxide inclusion and ferrite, positive thermal stress in the matrix surrounding the inclusion due to a high difference in thermal expansion coefficients and formation of an Mn-depleted zone in the adjacent matrix due to MnS precipitation.[5]

In general, non-metallic inclusions can be classified according to the timing of their formation as either primary or secondary inclusions. Primary inclusions are generated as a direct result of the deoxidation reactions at the steelmaking temperature whereas secondary inclusions form during the solidification process. In principle, primary inclusions can be removed by flotation. However, secondary inclusions are almost impossible to remove and can only be engineered to minimize their harmful effects on steel.

A previous study by Kim *et al.* investigated the precipitation behavior of secondary MnS inclusion on primary oxide

* Corresponding author: E-mail: jonah.gamutan@gmail.com
DOI: https://doi.org/10.2355/isijinternational.ISIJINT-2019-777

© 2020 ISIJ

inclusions under different cooling conditions in Si–Mn and Si–Mn–Ti deoxidized steels.[25,26] It was found that MnS precipitation was well manifested in furnace-cooled samples, in contrast to the water-quenched samples, due to longer solidification times and slower cooling rates. In addition, MnS precipitation behavior was found to vary depending on the composition of the primary oxide seed. When the primary oxide phase was composed of manganese silicate, MnS was found to precipitate in an embedded state. On the other hand, when the primary oxide phase was not composed of manganese silicate but rather of Ti_2O_3, MnS precipitated as a sulfide shell wrapping the primary inclusion.

In this study, transient inclusion behavior during solidification of the alloy, specifically at the solid-liquid coexistence temperature (T_s), was explored to achieve a better understanding of inclusion formation during steelmaking. In our previous study, we found out that due to the enrichment of solute elements in the liquid phase, precipitation of a secondary SiO_2-rich phase leads to the evolution of a complex type inclusion in Si-Mn deoxidized steel at the solid-liquid coexistence temperature.[27]

To further investigate the changes in morphology and composition of inclusions in Si–Mn deoxidized steel concerning MnS precipitation on an oxide inclusion for acicular ferrite formation, sulfur was added to the alloy system we examined earlier. Sulfur is widely known to have a very low solubility in the solid phase and can be largely segregated during solidification resulting in a large increase in the solidification range.[28,29] One of the prominent characteristics of the Fe–S binary alloy system is that it has a considerably wide two-phase region composed of δ-Fe and L above 1 365°C and γ-Fe and L above 968°C.[30] During cooling at this region, a segregation profile is expected to develop within the microstructure of the alloy as the liquid phase becomes richer in sulfur. These conditions may consequently lead to the nucleation of new inclusions or transformation of existing ones.[31]

Thus, with the increasing importance of controlling inclusions to achieve a desirable acicular ferrite microstructure in steel, MnS precipitation behavior on a primary MnO–SiO_2 inclusion in Fe–Mn–Si–O–S alloy system at the solid-liquid coexistence temperature was examined.

2. Experimental Method

To investigate the morphology and composition of oxide and sulfide inclusions in Si–Mn deoxidized steel during solidification, samples with varying sulfur addition at constant silicon and manganese contents were prepared in a vertical resistance furnace by holding at the solid-liquid coexistence temperature using a direct method of forming inclusions.

2.1. Preparation of the Alloy

About 25 g of electrolytic Fe with reagent grade metallic manganese flakes, silicon lumps, Fe_2O_3 and FeS powders were weighed and then placed inside an alumina crucible at the following initial compositions [Fe-1.1Mn-0.10Si-0.05O-S (mass%); 0.005%, 0.007%, 0.009%, 0.011%, 0.022%, 0.025%, 0.028% and 0.031% S]. The amount of manganese and silicon addition was chosen from our previous results based on having one of the highest complex inclusion formation ratios at the solid-liquid coexistence temperature. The prepared samples were then placed in an outer MgO crucible holder and then positioned in the constant temperature region of the vertical resistance furnace. Subsequently, the samples were heated using a pre-determined heating pattern under Ar gas atmosphere, flowing at 300 cm^3/min after passing through a gas drying unit. The actual temperature of the sample was monitored using a Pt-Rh thermocouple positioned just below the stage inside the furnace. After heating, the resulting alloys were quickly taken out of the furnace and quenched using Ar gas.

2.2. Heating Pattern

The heating pattern, as illustrated in **Fig. 1**, begins by heating the sample to 1 550°C for 2 hours to achieve equilibrium and allow for the formation of primary inclusions. Next, the temperature was gradually lowered to the solid-liquid coexistence temperature where it was held for 1 hour to allow for the formation of secondary inclusions to occur. After, the samples were then quickly taken out of the furnace and quenched.

Solid-liquid coexistence temperature (T_S) at different sulfur additions, wherein about 50% of the solidified alloy and 50% of the liquid alloy coexist, was estimated using the single point equilibrium module of Thermo-Calc Software. For example, stable phases and inclusions that form in Fe-1.1Mn-0.10Si-0.05O-0.007S (mass%) alloy system and their relative weights under equilibrium conditions are shown in **Fig. 2**. It was found that for this alloy system, solidification from a completely liquid state starts at about 1 531°C and ends at about 1 526°C. For the heating experiments, the solid-liquid coexistence temperature was determined to be about 1 526.97°C.

This value was also verified by calculating the liquidus and solidus temperatures of the alloy using the following equations derived by Miettinen *et al.*[32] and Gryc *et al.*,[33] respectively:

$$T_{liq}\,(^{\circ}\mathrm{C}) = 1\,538 - 11.66[\%Si] - 5.62[\%Mn] - 32.81[\%S]$$

$$T_{sol}\,(^{\circ}\mathrm{C}) = 1\,536 - 12.3[\%Si] - 6.8[\%Mn] - 183.9[\%S]$$

Calculated liquidus, solidus, and solid-liquid coexistence temperature values for all sulfur additions are shown in **Fig. 3**. It can be seen that the calculated solid-liquid coexistence temperature values lie well within the liquidus and solidus boundaries. In addition, the gap between the liquidus and solidus temperatures increases with increasing sulfur addition as described earlier.

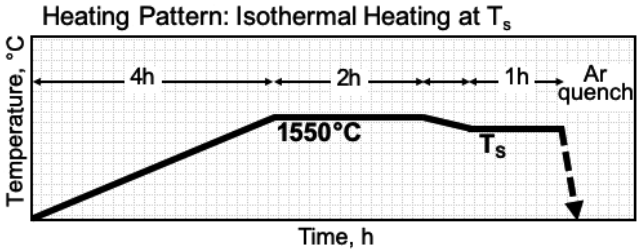

Fig. 1. Heating pattern used in this study.

© 2020 ISIJ

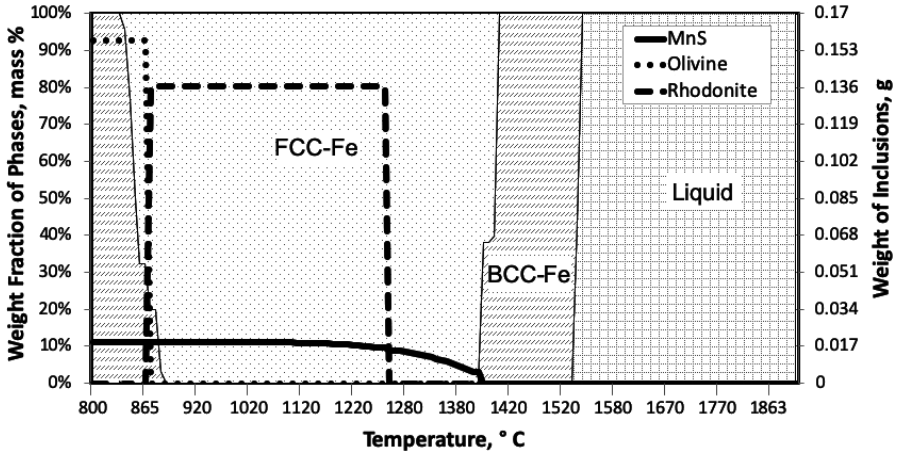

Fig. 2. Calculated 1.1Mn-0.10Si-0.05O-0.007S (mass%) single point equilibrium using Thermo-Calc (Olivine: Mn_2SiO_4, Rhodonite: $MnSiO_3$).

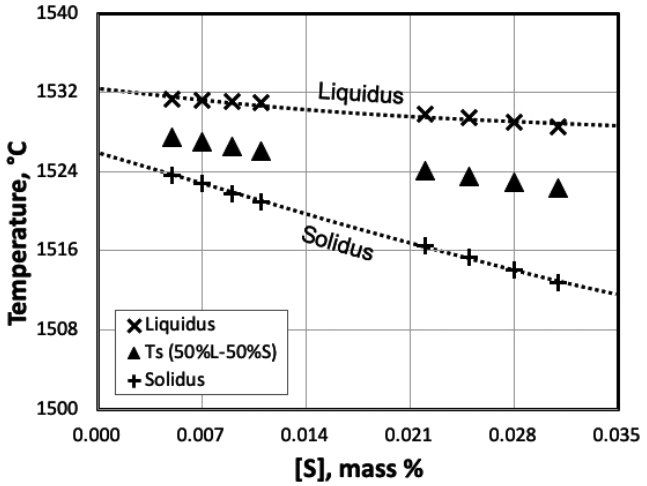

Fig. 3. Calculated solidus, liquidus and solid-liquid coexistence temperatures at different sulfur additions.

2.3. Characterization

The resulting metal phase composition was determined using ICP-AES (Inductively Coupled Plasma – Atomic Emission Spectroscopy) technique by dissolving about 1.0 g of the prepared alloy in 10 ml of aqua regia solution heated to 50–60°C for 3 hours. After complete dissolution of the alloy was confirmed through visual inspection, the resulting solutions were filtered and then analyzed for silicon and manganese contents.

Oxygen and sulfur contents of the alloys were determined using an inert gas fusion technique (LECO-ONH836) and a combustion infrared detection technique (LECO-CS844), respectively. For oxygen determination, 0.5 to 1.0-gram alloy samples were cut and polished using SiC paper up to #600 grit with ultrasonic bath cleaning in an anhydrous ethanol solution between every polishing step to remove surface contamination. For sulfur determination, 0.5 to 1.0-gram alloy samples were used.

Morphology and composition of inclusions were determined using SEM-EDS (Scanning Electron Microscopy with Energy Dispersive X-ray Spectroscopy) coupled with an image analysis technique to ensure reasonable measurements.[25] Alloy samples were longitudinally cut and hot-mounted in a carbon filler resin for easier grinding and polishing with a series of SiC paper from #120 grit up to #1 500 grit. Subsequently, inclusion size and morphology were assessed using the built-in image analysis tool in the SEM software. The composition of the inclusions was measured through EDS by analyzing a minimum of 30 inclusions with an acceleration voltage (AV) of 20 kV, a working distance (WD) of 15 mm and a spot size (SS) of 60 nm. At least 5 spots per inclusion were selected for point analysis. Iron and oxygen were excluded from the quantitative results to eliminate the influence of a pre-dominantly ferrous matrix and to avoid the inaccuracies associated with oxygen determination in this analysis. Obtained concentration values were normalized to 100% and reported in terms of mass percentage.

3. Experimental Results

3.1. Attainment of Equilibrium at 1 550°C

Before the heating experiments at the solid-liquid coexistence temperature, it is crucial to determine the necessary holding time to achieve equilibrium at 1 550°C first. To achieve this, three alloy samples of the Fe-1.1Mn-0.10Si-0.05O-0.007S (mass%) system were prepared under different reaction periods. The manganese, silicon, oxygen and sulfur contents of the resulting alloys were measured as shown in **Fig. 4**. No significant changes in the composition were observed at 2, 3 and 4 hrs of heating time. Silicon and manganese composition values were almost constant. Dissolved oxygen (91.60, 97.57 and 90.43 ppm) and sulfur (112.05, 111.38 and 114.90 ppm) contents were also found to be unchanging under different heating periods as indicated in Fig. 4. Hence, the necessary time to reach equilibrium for the Fe–Mn–Si–O–S system at 1 550°C was determined to be adequate at 2 hrs.

3.2. Metal Phase Composition at the Solid-liquid Coexistence Temperature

Fundamental alloy composition used in this study was selected based on the results from our previous study for having one of the highest complex inclusion formation ratios at the solid-liquid coexistence temperature. We found that to achieve a complex inclusion formation ratio greater than 60%, silicon to manganese ratio of 0.20 or higher is

© 2020 ISIJ

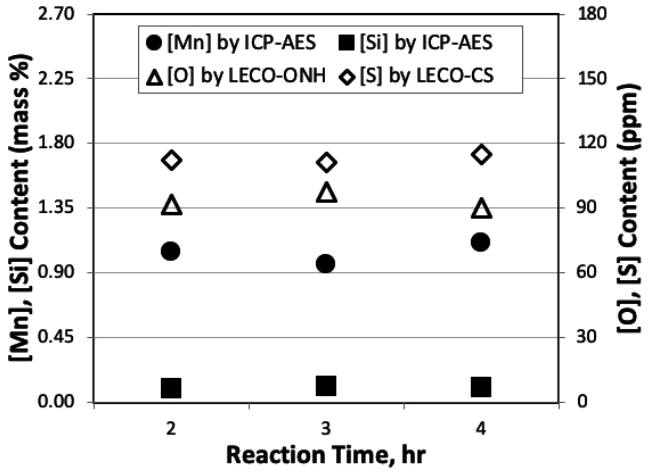

Fig. 4. [Mn], [Si], [O] and [S] contents at 1 550°C under different holding times.

Table 1. Chemical composition of the prepared alloy samples.

Sample	Metal Phase Composition			
	[Mn] mass%	[Si] mass%	[O] ppm	[S] ppm
0.005S	0.440	0.096	48.78	82.68
0.007S	0.434	0.104	62.78	94.51
0.009S	0.398	0.102	65.24	91.50
0.011S	0.437	0.104	57.56	108.23
0.022S	0.587	0.101	33.70	212.45
0.025S	0.613	0.108	31.46	193.08
0.028S	0.814	0.100	44.98	226.03
0.031S	0.777	0.136	36.38	240.60

necessary. This guarantees that a SiO_2-rich secondary inclusion phase will precipitate and coalesce with the primary MnO–SiO_2 phase, forming a complex type of inclusion.[27]

From this, sulfur addition was varied to further investigate the behavior of inclusion formation in Fe–Mn–Si–O–S alloy system during solidification. The composition of the resulting alloy phase after heating at the solid-liquid coexistence temperature are listed in **Table 1**. Manganese, silicon, and oxygen contents were kept relatively constant for all samples. Meanwhile, sulfur content increased from about 82.68 ppm to 240.60 ppm.

3.3. Inclusion Morphology and Composition

Representative morphology of inclusions that formed in samples with less than 0.011 mass% sulfur at the solid-liquid coexistence temperature is shown in **Fig. 5**. At low sulfur additions, complex inclusions with a darker SiO_2-rich inclusion phase embedded in a primary MnO–SiO_2 phase were observed in all samples. Average inclusion diameter per sample ranged from about 3.89 μm to 4.38 μm. MnO and SiO_2 concentration in the primary and secondary inclusion phases, classified as such according to the timing of their formation, were found to remain almost constant with increasing sulfur addition. Furthermore, approximately 2 mass% of sulfur was found dissolved in the inclusion. Precipitation of a SiO_2-rich secondary inclusion phase has been linked with the microsegregation of solute elements in the liquid phase at the solid-liquid coexistence temperature. During solidification, solute elements such as silicon and oxygen are known to enrich in the liquid phase as they are rejected from the solidified alloy, thus creating a favorable environment for the nucleation of silica.[34]

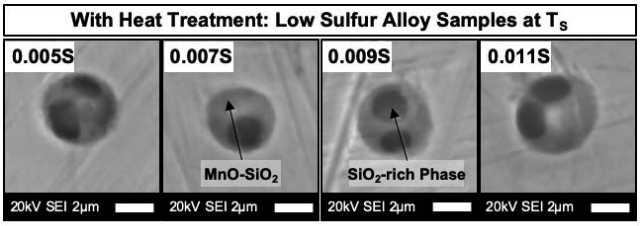

Composition (mass %)		0.005S	0.007S	0.009S	0.011S
Primary Inclusion Phase	(MnO)	50.53	49.05	49.96	49.20
	(SiO_2)	46.98	48.64	47.76	48.09
	(S)	2.49	2.31	2.28	2.71
Secondary Inclusion Phase	(MnO)	32.89	28.96	27.04	26.91
	(SiO_2)	65.61	69.39	71.54	71.30
	(S)	1.50	1.66	1.42	1.80
Ave. Inclusion Diameter, μm		3.95	4.06	4.38	3.89

Fig. 5. Typical inclusion morphology and composition in low sulfur samples (0.005 mass% to 0.011 mass% S) at the solid-liquid coexistence temperature.

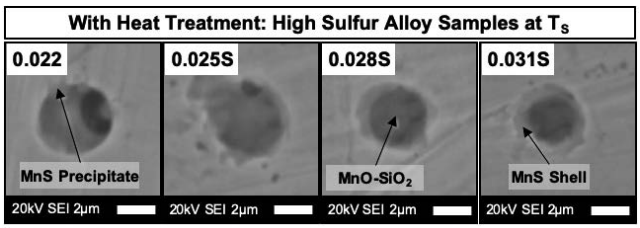

Composition (mass %)		0.022S	0.025S	0.028S	0.031S
Primary Inclusion Phase	(MnO)	51.60	52.01	50.84	50.47
	(SiO_2)	41.81	41.61	41.30	40.64
	(S)	6.58	6.39	7.87	8.90
Secondary SiO_2-rich Phase	(MnO)	31.55	32.35	32.35	34.70
	(SiO_2)	63.40	63.22	58.46	59.82
	(S)	5.05	4.42	9.19	5.49
Secondary MnS	(Mn)	72.28	71.75	69.85	68.33
	(S)	27.72	28.25	30.15	31.67
Ave. Inclusion Diameter, μm		4.11	4.43	3.52	3.24

Fig. 6. Typical inclusion morphology and composition in high sulfur samples (0.022 mass% to 0.031 mass% S) at the solid-liquid coexistence temperature.

On the other hand, in alloy samples with higher than 0.022 mass% sulfur addition, precipitation of a lighter phase along the boundary of the primary MnO–SiO_2 inclusion and the steel matrix was observed as presented in **Fig. 6**. Average inclusion diameter per sample ranged from about 3.24 μm to 4.43 μm. Growing with increasing sulfur addition, the lighter colored precipitate completely wrapped the primary MnO–SiO_2 inclusion at about 0.031 mass% sulfur addition forming a shell around it. Elemental mapping and line scan results showed this lighter precipitate phase to be comprised largely of MnS. As illustrated in **Fig. 7**, the primary inclusion is composed primarily of manganese, silicon, and sulfur whereas, along the boundary of the inclusion, sulfur was found to have higher concentrations, indicating

© 2020 ISIJ

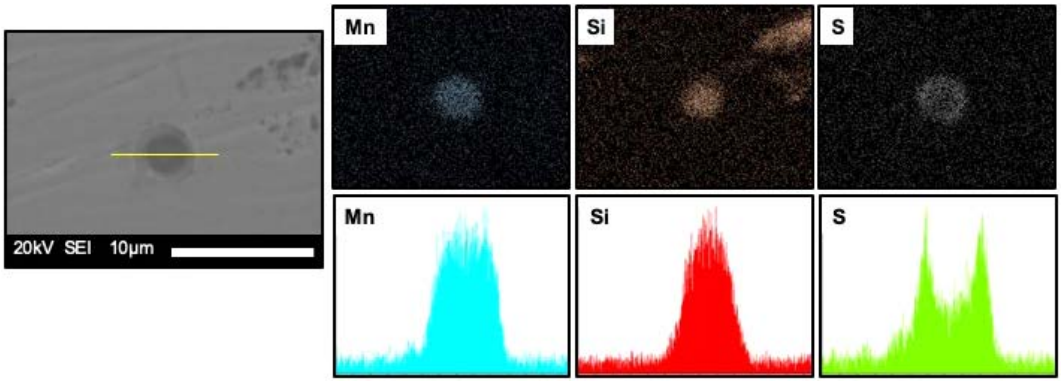

Fig. 7. Elemental map and line scan of a typical inclusion in 0.031S sample by SEM-EDS. (Online version in color.)

MnS formation. These results were found to diverge from previous findings by Kim *et al.* citing that secondary MnS precipitate forms in an embedded state, not as a shell, on a manganese silicate-based primary inclusion. This difference is largely attributed to the prolonged holding time at the solid-liquid coexistence temperature in contrast to the continuous cooling conditions employed by Kim *et al.*[25] Similarly, MnO and SiO_2 concentration in the primary and secondary inclusion phases were found to remain almost constant even with increasing sulfur addition. Compared to low sulfur alloy samples, a higher sulfur content of approximately 6 to 9 mass% was found dissolved in the inclusion as shown in Fig. 6.

In addition to the above-mentioned changes in inclusion morphology and composition at the solid-liquid coexistence temperature, it was also observed that the secondary SiO_2-rich precipitate began to disappear from the primary inclusion phase in the majority of the inclusions with increasing sulfur addition. At 0.022 mass% sulfur addition, almost all inclusions still showed the coexistence of the secondary SiO_2-rich inclusion and the secondary MnS precipitate on a primary MnO–SiO_2 inclusion. At 0.031 mass% sulfur addition, however, the darker SiO_2-rich inclusion phase failed to precipitate in almost all of the inclusions observed. From our previous findings, primary MnO–SiO_2 inclusion formed above the liquidus temperature while the secondary SiO_2-rich inclusion formed as a result of solute microsegregation and enrichment at the liquid phase at the solid-liquid coexistence temperature. Eventually, with the help of natural convection in the alloy, the existing primary MnO–SiO_2 inclusion and the secondary SiO_2-rich inclusion coalesced to form a complex type of inclusion. In the current Fe–Mn–Si–O–S alloy system, precipitation of MnS along the interface of the primary MnO–SiO_2 inclusion and the molten alloy was assumed to physically prevent coalescence and agglomeration of existing inclusions. Hence, SiO_2 precipitates remained in the alloy in an independent state, as it was observed in all of the prepared alloy samples.

3.4. Timing of Inclusion Formation

In order to distinguish between the primary and secondary inclusions according to the timing of their formation, 0.007S sample was heated and quenched from different stages of the designed heating pattern. The first one was quenched after heating for two hours at 1 550°C and the second one was quenched from just above the liquidus temperature.

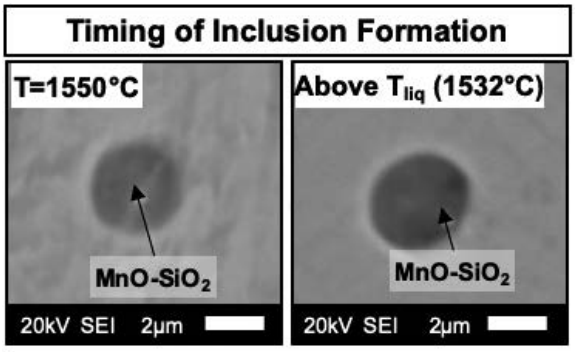

Composition (mass %)	Temperature 1550°C	1532°C
(MnO)	52.33	55.11
(SiO_2)	44.85	41.82
S	2.83	3.07
Diameter, μm	3.20	3.71

Fig. 8. Typical inclusion morphology and composition of 0.007S sample at 1 550°C and just above the liquidus temperature at 1 532°C.

As shown in **Fig. 8**, the inclusions at 1 550°C and 1 532°C, which is just right before solidification begins, are predominantly characterized by simple MnO–SiO_2 inclusions with some dissolved amount of sulfur. The MnO–SiO_2 inclusions, are hence classified as primary inclusions that formed as a direct outcome of the deoxidation process. Further, no darker-colored SiO_2-rich phase was observed at these temperature conditions. Since it did not appear before solidification, the SiO_2-rich phase that was observed at the solid-liquid coexistence temperature are therefore classified as secondary inclusions generated during the solidification process.

4. Discussion

4.1. Thermodynamic Consideration

At near-equilibrium conditions, inclusion formation at the solid-liquid coexistence temperature in the Fe-1.1Mn-0.10Si-0.05O-S (mass%) alloy system can be described from a thermodynamic point of view using the ternary MnO–SiO_2–MnS phase equilibrium diagram illustrated in

© 2020 ISIJ

Fig. 9. This diagram, originally taken from Hasegawa *et al.*, reveals the liquidus lines for the MnO–SiO_2–MnS ternary system at 1 450°C.[35] Although the actual temperature used in this study was slightly higher than these values, the difference can be neglected to roughly explain the thermodynamic behavior of the inclusions.

In low sulfur samples, the equilibrium lies initially at Point 1, which is at SiO_2 saturation. During the isothermal holding of the samples at the solid-liquid coexistence temperature, a secondary SiO_2-rich inclusion phase precipitated homogeneously in the melt due to microsegregation and later became embedded in the primary MnO–SiO_2 inclusion. Homogeneous nucleation of SiO_2 was confirmed by the presence of independent SiO_2 inclusions in the alloy. Sulfur, on the other hand, remained in a dissolved state in the inclusion. With more sulfur addition, the equilibrium shifted to Point 2, where the inclusion became doubly saturated with MnS and SiO_2, as demonstrated for instance in 0.022S sample. SiO_2-rich inclusion remained embedded in the primary oxide phase while new MnS inclusion precipitated along the boundary of the inclusion and the steel matrix.

Inclusions can either homogeneously nucleate in the melt or heterogeneously on existing impurities. In this case, precipitation of MnS on existing MnO–SiO_2 inclusion can be regarded as heterogeneous nucleation due to the absence of independent MnS inclusions in the alloy matrix. During this process, the surface of an existing inclusion becomes a highly favorable site for the nucleation of new inclusions due to lower effective surface energy that weakens the free energy barrier and enables nucleation. The likelihood of heterogeneous nucleation to occur is higher than homogeneous nucleation due to lesser nucleation energy that is needed.[31]

With much higher sulfur addition such as in 0.031S sample, although the absence of a SiO_2-rich phase was observed and only the secondary MnS phase existed in the primary MnO–SiO_2 inclusion, the equilibrium was assumed to remain in Point 2 since independent SiO_2 inclusions were still present in the alloy. These observations indicate that the presence of an MnS shell prevents the secondary SiO_2 precipitates to coalesce with the existing MnO–SiO_2 inclusion at the solid-liquid coexistence temperature. Hence, almost all of the observed inclusions lacked the darker SiO_2-rich phase.

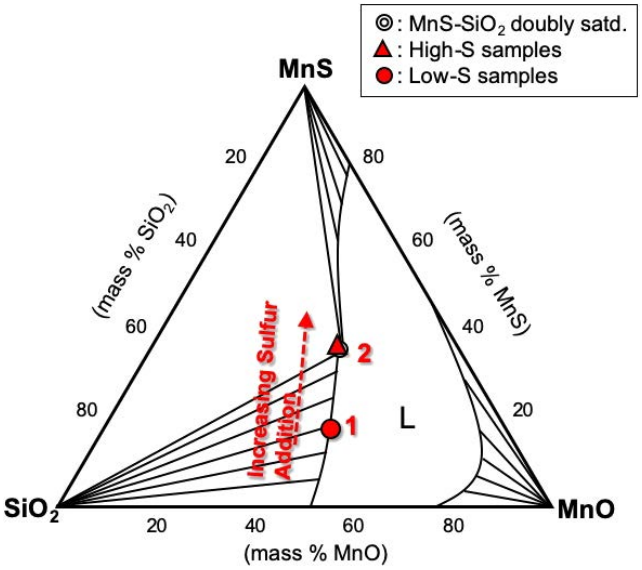

Fig. 9. Liquidus for the MnO–SiO_2–MnS ternary system at 1 450°C.[35] (Online version in color.)

4.2. Inclusion Formation Mechanism and Control

In this study, inclusions generated after isothermal holding at the solid-liquid coexistence temperature can be classified into three categories – MnO–SiO_2 with an embedded SiO_2-rich phase, MnO–SiO_2 with both SiO_2-rich phase and MnS, and MnO–SiO_2 with an MnS shell. As mentioned in the earlier sections, SiO_2 precipitated homogeneously in the molten alloy as a result of solute enrichment and later became embedded in MnO–SiO_2 while MnS precipitated heterogeneously on the surface of the existing MnO–SiO_2 due to the lowering of the interfacial surface energy.

These changes in the morphology and composition of inclusions are highly correlated with the dissolved sulfur content in the steel as shown in **Fig. 10**. Precipitation ratio was calculated as follows:

$$Precipitation\ Ratio = \frac{No.\ of\ inclusions\ with\ precipitate}{Total\ no.\ of\ inclusions} \times 100\%$$

wherein precipitate pertains to either of SiO_2 or MnS divided by the total number of inclusions observed. MnS precipitation ratio was found to increase with increasing sulfur content. Data on MnS precipitation ratio in Si–Mn deoxidized steel from Kim *et al.* and Wakoh *et al.* also showed similar behavior, although higher precipitation ratio was obtained at lower sulfur contents.[26,36] This can be ascribed to the difference in composition and heating and cooling conditions employed. For instance, [Si]/[Mn] ratios by Wakoh *et al.* ranged from about 0.007 to 0.20. Furthermore, about 0.09 to 0.011 mass% of carbon was used in the previous studies cited whereas carbon is absent in the current alloy system. MnS precipitation is more likely to occur in the presence of carbon due to increased sulfur activity as a result of a strong thermodynamic interaction between the two.[37]

In the same way, a previous investigation by Wakoh *et al.* cited that MnS precipitation ratio is influenced by the composition of the MnO–SiO_2 seed. The MnS precipita-

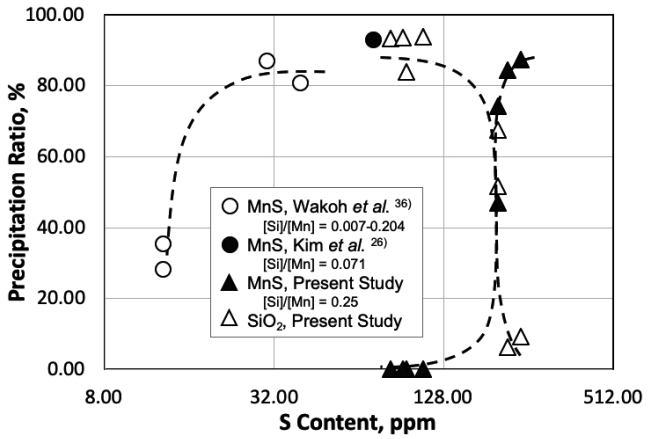

Fig. 10. Changes in MnS and SiO_2 precipitation ratio with sulfur content.

© 2020 ISIJ

tion ratios were found to increase in occasions when the $MnO–SiO_2$ seed had a lower melting temperature, starting from about 53 mass% MnO and peaking at about 73 mass% MnO.[38] In this study, MnO ratio in the primary oxide seed ranged only from about 50 to 55 masss%, hence the noticeable difference in the experimental MnS precipitation ratios. Further, precipitation of MnS can also be rationalized from the viewpoint of microsegregation. Gui *et al.* state that sulfur content in steel has a great impact on the precipitation of MnS.[39] At 0.005 mass% sulfur, MnS precipitates only after the alloy has completely solidified at about 1 417°C. Whereas at higher 0.35 mass% sulfur, MnS precipitation starting temperature moved up to the two-phase region (δ-Fe and L) at about 1 497°C. This is greatly influenced by the redistribution of manganese and sulfur in the liquid and solid phases during the solidification process, as it was also confirmed experimentally in this study – no MnS precipitates were observed in low sulfur samples (0.005 to 0.011 mass% S) while MnS precipitation was well manifested in high sulfur samples (0.022 to 0.031 mass% S).

SiO_2 precipitation ratio, on the other hand, was found to decrease with increasing sulfur content. Generally speaking, MnS and SiO_2 precipitation behavior on a primary $MnO–SiO_2$ seed appeared to be inversely related to each other. These results indicate that controlling sulfur content in the alloy can more or less predict the type of precipitate that forms in Si–Mn deoxidized steel at the solid-liquid coexistence temperature such as in the case of aiming for an acicular ferrite microstructure with the precipitation of MnS on an oxide inclusion.

5. Conclusion

Inclusion formation behavior in Fe–Mn–Si–O–S alloy system with varying sulfur addition after isothermal holding at the solid-liquid coexistence temperature was experimentally observed and considered in this study as follows:

a) Low sulfur samples (0.005 to 0.011 mass% S): Homogeneous precipitation of SiO_2, which was later on embedded on a primary $MnO–SiO_2$ inclusion. Sulfur remained dissolved in the inclusion (2 to 4 mass% S) and no MnS precipitation was observed.

b) High sulfur samples (0.022 to 0.031 mass% S): Heterogeneous precipitation of an MnS shell around a primary $MnO–SiO_2$ inclusion with a higher amount of dissolved sulfur (7 to 13 mass% S). This was coupled with the disappearance of the secondary SiO_2-rich phase with increasing sulfur addition.

MnS precipitation behavior with sulfur addition was explained from a thermodynamic point of view using the $MnO–SiO_2–MnS$ ternary system considering near-equilibrium conditions. In addition, changes in morphology and composition were elucidated as a result of manganese and sulfur enrichment in the liquid phase that led to heterogeneous MnS precipitation on $MnO–SiO_2$ inclusion at the solid-liquid coexistence temperature.

REFERENCES

1) N. Ånmark, A. Karasev and P. G. Jönsson: *Materials*, **8** (2015), 751.
2) A. L. V. da Costa e Silva: *J. Mater. Res. Technol.*, **7** (2018), 283.
3) A. L. V. da Costa e Silva: *J. Mater. Res. Technol.*, **8** (2019), 2408.
4) J. Takamura and S. Mizoguchi: Proc. 6th Int. Iron and Steel Congr., Vol. 1, ISIJ, Tokyo, (1990), 591.
5) D. S. Sarma, A. V. Karasev and P. G. Jönsson: *ISIJ Int.*, **49** (2009), 1063.
6) D. Loder, S. K. Michelic and C. Bernhard: *J. Mater. Sci. Res.*, **6** (2017), 24.
7) T. K. Lee, H. J. Kim, B. Y. Kang and S. K. Hwang: *ISIJ Int.*, **40** (2000), 1260.
8) H. Nako, Y. Okazaki and J. G. Speer: *ISIJ Int.*, **55** (2015), 250.
9) D. Zhang, Y. Shintaku, S. Suzuki and Y. Komizo: *Metall. Mater. Trans. A*, **43** (2012), 447.
10) D. Zhang, Y. Shintaku, S. Suzuki and Y. Komizo: *J. Mater. Sci.*, **47** (2012), 5524.
11) D. Zhang, H. Terasaki and Y. Komizo: *Acta Mater.*, **58** (2010), 1369.
12) T. Furuhara, J. Yamaguchi, N. Sugita, G. Miyamoto and T. Maki: *ISIJ Int.*, **43** (2003), 1630.
13) T. Furuhara, T. Shinyoshi, G. Miyamoto, J. Yamaguchi, N. Sugita, N. Kimura, N. Takemura and T. Maki: *ISIJ Int.*, **43** (2003), 2028.
14) R. A. Ricks, P. R. Howell and G. S. Barritte: *J. Mater. Sci.*, **17** (1982), 732.
15) Ø. Grong, A. O. Kluken, H. K. Nylund, A. L. Dons and J. Hjelen: *Metall. Mater. Trans. A*, **26** (1995), 525.
16) B. L. Bramfitt: *Metall. Trans.*, **1** (1970), 1987.
17) O. Grong and D. K. Matlock: *Int. Met. Rev.*, **31** (1986), 27.
18) D. Brooksbank and K. W. Andrews: *J. Iron Steel Inst.*, **210** (1972), 246.
19) S. Ohkita and Y. Horii: *ISIJ Int.*, **35** (1995), 1170.
20) J. L. Lee and Y. T. Pan: *ISIJ Int.*, **35** (1995), 1027.
21) H. Mabuchi, R. Uemori and M. Fujioka: *ISIJ Int.*, **36** (1996), 1406.
22) K. Yamamoto, T. Hasegawa and J. Takamura: *ISIJ Int.*, **36** (1996), 80.
23) J. S. Byun, J. H. Shim, Y. W. Cho and D. N. Lee: *Acta Mater.*, **51** (2003), 1593.
24) S. J. Jones and H. K. D. H. Bhadeshia: *Metall. Mater. Trans. A*, **28** (1997), 2005.
25) H. S. Kim, H. G. Lee and K. S. Oh: *ISIJ Int.*, **42** (2002), 1404.
26) H. S. Kim, H. G. Lee and K. S. Oh: *Metall. Mater. Trans. A*, **32** (2001), 1519.
27) J. L. Gamutan, T. Miki and T. Nagasaka: *ISIJ Int.*, **60** (2020), 84.
28) M. Wintz, M. Bobadilla, J. Lehmann and H. Gaye: *ISIJ Int.*, **35** (1995), 715.
29) O. Kubaschewski: Iron-Binary Phase Diagrams, Springer-Verlag, Berlin, (1982), 125.
30) H. Okamoto: Phase Diagrams of Binary Iron Alloys, ASM International, Materials Park, OH, (1993), 364.
31) D. You, S. K. Michelic, P. Presoly, J. Liu and C. Bernhard: *Metals*, **7** (2017), 460.
32) J. Miettinen and A. A. Howe: *Ironmaking Steelmaking*, **27** (2000), 212.
33) K. Gryc, B. Smetana, M. Žaludová, K. Michalek, P. Klus, M. Tkadlečková, L. Socha, J. Dobrovská, P. Machovčák, L. Válek, R. Pachlopnik and B. Chmiel: *Mater. Technol.*, **47** (2013), 569.
34) T. Fujisawa, M. Nomura and H. Sakao: *Trans. Iron Steel Inst. Jpn.*, **21** (1981), 624.
35) A. Hasegawa, K. Morita and N. Sano: *Tetsu-to-Hagané*, **81** (1995), 1109 (in Japanese).
36) M. Wakoh, T. Sawai and S. Mizoguchi: *ISIJ Int.*, **36** (1996), 1014.
37) Y. Tanaka, F. Pahlevani, S. C. Moon, R. Dippenaar and V. Sahajwalla: *Sci. Rep.*, **9** (2019), 10096.
38) M. Wakoh, T. Sawai and S. Mizoguchi: *Tetsu-to-Hagané*, **78** (1992), 1697 (in Japanese).
39) L. Gui, M. Long, H. Chen, D. Chen, H. Duan, Y. Huang and T. Liu: *J. Mater. Res.*, **33** (2018), 3490.

© 2020 ISIJ